MJFAS
Malaysian Journal of Fundamental and Applied Sciences

RESEARCH ARTICLE

Identification of the Subsurface Structure of Gamalama Volcano (Ternate City) Using HVSR Inversion Methods

Andri Wijaya Bidang[a,b]*, Safri Burhanuddin[b], Agustya Adi Martha[c]

[a]The Agency for Meteorology, Climatology and Geophysics, 10610 Jakarta, Indonesia; [b]Department of Geology, Faculty of Engineering, Hasanuddin University, 92171 Gowa, South Sulawesi, Indonesia; [c]The National Research and Innovation Agency, 10340 Jakarta, Indonesia

Abstract The Gamalama volcano slopes and coastal regions, inhabited by 90% of Ternate City's 200,000 residents have been designated as strategically vital for housing North Maluku's administrative, economic, and cultural core, creating compounded risks during volcanic activity. To quantify these risks, the volcanic subsurface was systematically profiled using passive seismic methods, with microtremor-derived Horizontal to Vertical Signal Ratio (HVSR)inversions being utilized to detect (1) sediment-basement interfaces and (2) concealed fault systems relevant for mitigation measures in Ternate's urban sector. The sediment thickness variations revealed the presence of previously unidentified fault structures, designated as H, I, J, K, and L, which were detected beneath densely populated urban areas.

Keywords: Gamalama Volcano, HVSR inversion, layer thickness, microtremor, fault.

Introduction

Mount Gamalama, located on Ternate Island, has been identified as a stratovolcano with an elevation of 1,715 meters above sea level and surrounded by areas of high population density. The hazards associated with this volcano have been recognized as not only arising from primary volcanic products such as lava flows, pyroclastic material, and ballistic projectiles, but also from secondary hazards such as lahars, landslides, and debris flows. The vulnerability of Ternate's population has been further exacerbated by the limited accessibility of evacuation routes, insufficient transportation infrastructure, and restricted emergency response capacity Syiko, T. A [9]. Consequently, an understanding of the subsurface condition of the volcanic edifice has been regarded as essential for the development of disaster mitigation strategies.

***For correspondence:**
suwanna.p@rmutsv.ac.th

Received: 2 July 2025
Accepted: 18 Sept. 2025

The formation of Gamalama has been attributed to the convergence of the Halmahera continental Plate with the subduction of the Molucca Sea oceanic Plate, which has resulted in the creation of the Halmahera subduction zone and its associated volcanic arc [1], [2], [3]. Within the documented historical record, 66 eruptions since 1510 have been reported, and a shift in eruptive style from magmatic to phreatic has been observed since 2003 [2], [4]. The magma composition has been classified as basaltic-dominated Kunrat[2] as well as andesitic–basaltic in character [5], indicating the potential for both effusive and explosive eruptions. Hydrothermal systems produced through magmatic gas–groundwater interaction have been linked to phreatic activity [6], [7], while the permeability of summit fracture networks has been identified as a critical factor controlling eruptive thresholds [2].

The importance of subsurface conditions in influencing hazard impact has been highlighted by earlier research. A proportional relationship between sediment thickness and earthquake damage intensity has been established in affected regions [8]. Geological structures such as faults and strike-slip zones have been shown to enhance permeability by creating interconnected fracture systems, which in turn facilitate magma ascent, fluid circulation, and volcanic gas emission [9], [10], [11]. In this regard, subsurface

characterization has been widely conducted through the Horizontal-to-Vertical Spectral Ratio (HVSR) method and its inversion, which have been validated for mapping sedimentary thickness, resonant frequencies, and seismic vulnerability [12]. The accuracy of these methods has been further confirmed by consistency with one-dimensional soil model amplification peaks, borehole measurements, and shear-wave surveys, with applicability demonstrated for sedimentary and soil layers up to approximately 100 meters deep [13], [14], [15]. As such, HVSR and HVSR inversion have been acknowledged as reliable techniques for subsurface investigations in complex geological environments [12], [16], [17], [18].

Although Mount Gamalama has exhibited frequent eruptive activity, comprehensive subsurface investigations have remained scarce. In particular, studies addressing the characterization of shear-wave velocity (Vs) structures have not been sufficiently conducted. To date, no detailed application of HVSR inversion techniques has been reported for this volcano. This absence is considered a critical research gap, since Vs characterization is essential for estimating site resonance, evaluating local seismic vulnerability, and assessing the structural stability of the volcanic edifice. Therefore, the present study has been designed to address this deficiency by investigating the subsurface structure of Mount Gamalama through the application of HVSR and HVSR inversion methods. By filling this gap, geological risk assessment can be enhanced, urban development planning in Ternate City can be better informed, and disaster mitigation strategies can be reinforced to reduce potential losses in both human lives and infrastructure.

Materials and Methods

HVSR (Horizontal to Vertical Spectral Ratio)

The dominant resonance frequency is extracted from the maximum observed H/V spectral ratio, where site amplification effects are quantified through spectral peak analysis. For visualization purposes, the Geopsy software package is employed to plot the horizontal-to-vertical spectral ratio as a function of frequency (HVSR diagram). The relationship between the microtremor H/V spectral ratio at frequency and wave motion components is expressed by the following empirical equation:

$$H/V(f) = \sqrt{\frac{|H_{NS}(f)|^2 + |H_{EW}(f)|^2}{|V_{UD}(f)|^2}} \quad \ldots(1)$$

Where $H_{NS}(f)$ and $H_{EW}(f)$ represent a fourier transform horizontal component frequencies, while $V\_UD\ (f)$ denotes a fourier transform vertical component frequency [12]. The obtained H/V spectral ratio is then processed through HVSR inversion.

The extraction of subsurface structural information is achieved through H/V spectrum inversion applied to dispersive waves (e.g., Rayleigh waves), with the H/V curves being derived from microtremor data

HVSR Inversion

The application of the Neighbourhood Algorithm (NA) in HVSR inversion is acknowledged not only as a means of global search but also as a Bayesian inference framework, in which ensembles are utilized to more effectively assess solution uncertainty plays a decisive role in interpretation. The primary process in this algorithm is the creation of new samples through uniform resampling within selected Voronoi cells. The underlying rationale is that the misfit value of a model is regarded as reflective of the entire area within its corresponding Voronoi cell. Consequently, during each iteration, new sample points are concentrated around models demonstrating the best data-fitting performance. In this manner, insights accumulated from prior models are utilized to adapt and guide the algorithmic search process [19].

This study was conducted at Mount Gamalama, encompassing 123 measurement points randomly distributed across urban and residential areas, each measurement point is separated 200 - 500 meters apart from the others. Ambient noise signals derived from natural sources (e.g., ocean waves, wind, and industrial machinery), were collected as microtremor data with horizontal and vertical components below 20Hz [15]. The 3-component Seismograph (0.01 – 100 Hz frequency range) was utilized for data acquisition, with each point measured for 30-45 minutes [20]

Figure 1. The 3-component Seismograph (Lunitex)

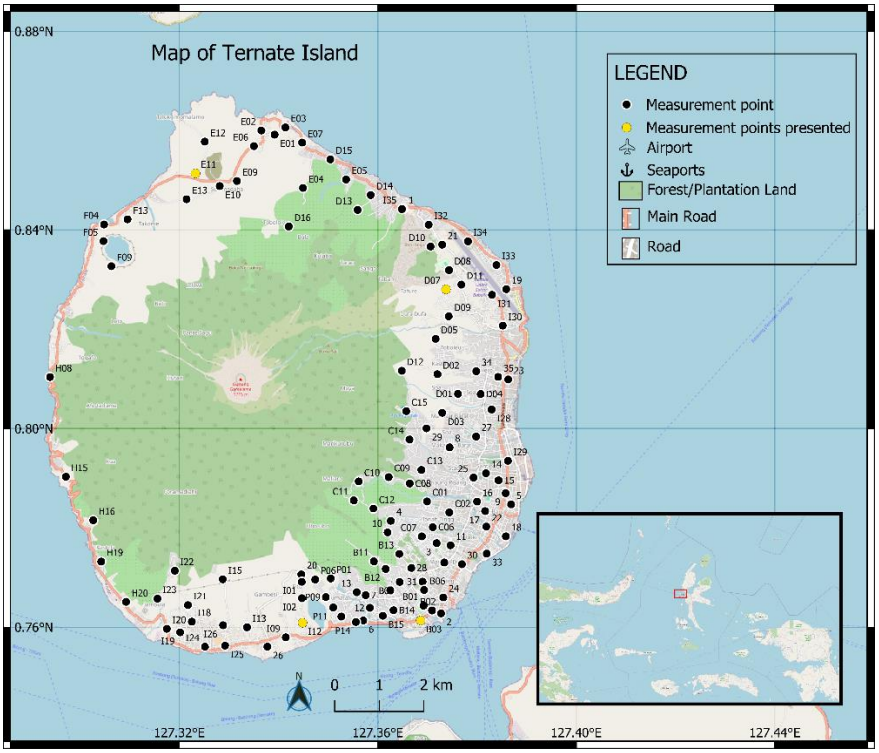

Figure 2. Research measurement point

The data processing procedure is executed in sequential phases:

1. The HVSR analysis comprises
   - Extraction of horizontal/vertical component signals
   - Application of <25 Hz low-pass filtering
   - Utilization of ≥20 times windows
   - Implementation of Konno-Ohmachi smoothing [20], [21], [22].

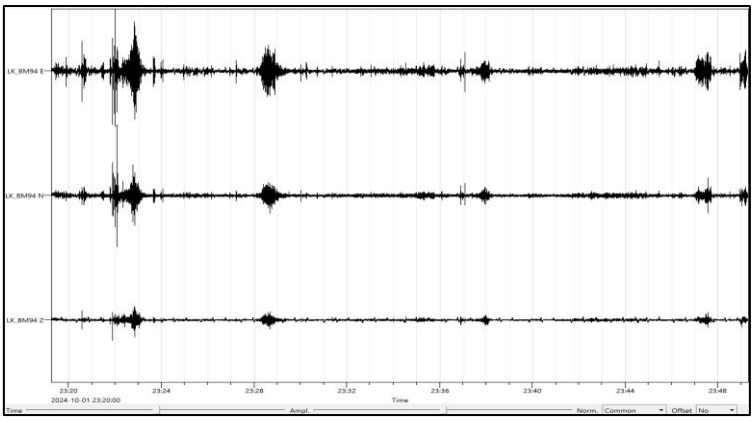

Figure 3. Microtremor signal at point D07

2. H/V Spectrum Inversion

The H/V Spectral Ratio data are then inverted using Dinver Surface Wave Inversion software with Ellipticity curve [22] to obtain the shear wave velocity (V_S) model and subsurface layer thickness at each measurement point. The methodological approach adopted in this work is based on the Neighbourhood Algorithm.

The initial model parameters consist of Compressional wave velocities ($V_{P0}, V_{P1}, V_{P2}, V_{P3}$) ranging from 200 m/s to 5000 m/s, Poisson's ratio between 0.2 and 0.5, Shear wave velocities ($V_{S0}, V_{S1}, V_{S2}, V_{S3}$) from 50 m/s to 3500 m/s, Minimum bulk density in sedimentary rocks (sandstone) of 2000 kg/m³ (Baker Atlas Log Interpretation Charts, 1985) [23].

Site classification by V_S30 [24]:

Table 1. Site Classification based on V_S30

Classification	V_S (m/s)
SA (Hard Rock)	>1500
SB(Rock)	750 – 1500
SC (Hard, Very compacted Soil, Soft Rock)	350 – 750
SD (Medium Soil)	175 – 350
SF (Soft soil)	<175

The HVSR inversion is performed to derive shear wave velocity profiles for each subsurface layer within a 30-meter depth limit, where all layers are assumed to be dense, homogeneous, and isotropic (Figure 4). Through this process, consistency between the soil layer model and observational data is maximized by systematically minimizing the misfit value, following established inversion methodologies that optimize the match between theoretical and measured spectral ratios [14], [25].

Layer Thickness Interpolation

Subsurface layer thickness data are interpolated using the kriging method to construct a spatial distribution model, where this approach is preferred due to its demonstrated advantages: (1) spatial structure (autocorrelation) is systematically accounted for, (2) prediction error estimates (variance) are provided, (3) flexibility with diverse data types is ensured, (4) optimal performance with sparse datasets is achieved, (5) directional variations (anisotropy) are effectively handled, and (6) applicability to complex geological scenarios is maintained [26].

The interpolation is performed using Surfer software (see Figures 8-15), with subsequent analysis involving the addition of 19 cross-sections to identify suspected fault lines in Ternate Island. The cross-section locations are determined based on: (1) the presence of potentially hazardous faults near urban, and (2) strategic placement at dense measurement points to enhance interpolation accuracy. This methodological approach is designed to optimize fault detection while maintaining spatial data integrity. A systematic explanation is provided for the frequency-soil characteristics relationship as classified by Kanai-Omote-Nakajima [27].

Table 2. Kanai-Omote-Nakajima soil classification

Soil Classification	$f_0\ (Hz)$	Specification	Description
Type I	6,667 - 20	Tertiary or older rocks. Consists of hars sandy rocks, gravel, etc	Surface sediment thickness is very thin, dominatedby hard rocks
Type II	4,0 – 6,667	Alluvial rock, with a thickness of 5 meters. Consists of sandy gravel, sandy hard clay, loam, etc	Surface sediment thickness is medium, about 5-10 meters
Type III	2,5 – 4,0	Alluvial rocks with a thickness of > 5 meters. Consists of sandy gravel, sandy hard clay, loam, etc	Surface sediment is thick about 10-30 meters
Type IV	<2,5	Alluvial rock, formed by delta sedimentation, top soil, mud, etc, a thickness ≥30 meters	Surface sediment is very thick

4. Cross-sectional analysis

The construction of cross-sections was performed by integrating interpolation results with Google Earth satellite imagery data, where subsurface structural profiles were systematically generated to identify potential fault structures. The cross-sectional analysis was specifically designed to visualize vertical variations in geological formations.

Results and Discussion

These observation points, sampled from various surface locations comprising rock and sediment layers, provide a basis for further discussion.

The D07 is characterized by young lava deposits at the surface, with flat topography and no settlements observed in the field [5]. The Subsurface lithology consists of coarse, subangular to rounded basaltic-andesite and andesite rocks within an unconsolidated matrix of mud and sand. At measurement point D07 (Mount Gamalama, Ternate City, Indonesia), the natural resonance frequency (f_c) of 3.58 Hz is identified, corresponding to alluvial rock/sandy gravel deposits (Table 2; Fig. 4a). The shear wave velocity profile is delineated as: (1) 464 m/s at shallow depths (≤3 m), classified as hard soils/soft rocks; (2) 1231 m/s at intermediate depths (3-28 m), representing rock; and (3) 2730 m/s at greater depths (28-30 m), indicative of hard rock formations (Table 1; Fig. 4b).

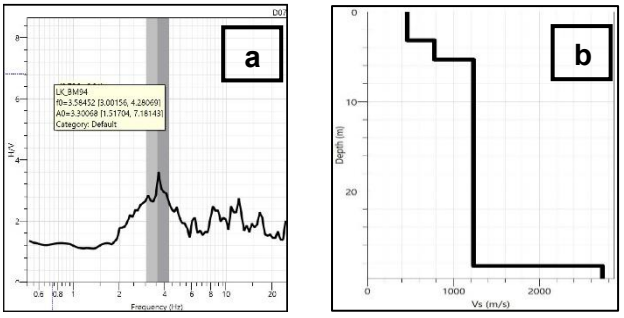

Figure 4. Observations at point D07. (a) of the HVSR Spectrum. (b) V_S model

The B03 is characterized by soft alluvium sediments, sand, and gravel deposits, with flat topography and surrounding residential settlements. At measurement point B03 (Gamalama Mt., Ternate City, Indonesia), the natural resonance frequency (f_c) of 0.72 Hz is identified, corresponding to alluvial rock/delta sedimentation/topsoil/mud deposits (Table 2; Fig. 5a). The shear wave velocity profile is delineated as follows: (1) 215 m/s at shallow depths (≤1 m), classified as medium soil; (2) 373 m/s at intermediate depths (1–3 m), representing hard/stiff soil and soft rock; (3) 528 m/s at greater depths (3–29 m), indicating hard/stiff soil and soft rock; and (4) 960 m/s at the deepest layer (29–30 m), consistent with competent rock (Table 1; Fig. 5b).

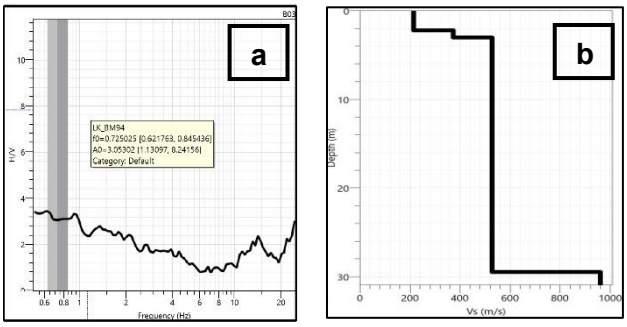

Figure 5. Observations at point B03. (a) HVSR spectrum. (b) V_S Model

The E11 is characterized by vesicular andesite block lava erupted in 1763, with flat topography comprising roads and forested land. At measurement point E11 (Gamalama Mt., Ternate City, Indonesia), the natural resonance frequency (f_c) of 5.78 Hz is identified, corresponding to alluvial rocks/sandy gravel/sandy hard deposits (Table 2; Fig. 6a). The shear wave velocity profile is delineated as follows: (1) 89 m/s at shallow depths (<1 m), classified as soft soil; (2) 245 m/s at depths of 1–6 m, representing medium soil; (3) 589 m/s at intermediate depths (6–25 m), indicating hard soil/soft rock; and (4) 2650 m/s at greater depths (25–30 m), consistent with hard rock formations (Table 1; Fig. 6b).

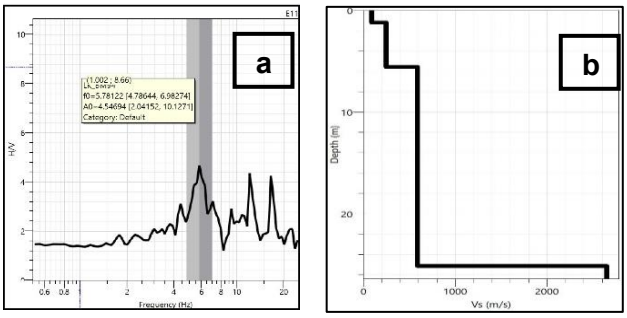

Figure 6. Observations at point E11. (a) HVSR spectrum. (b) V_SModel

The I12 is characterized by reworked pyroclastic deposits consisting of weakly consolidated ash, lapilli tuff, and pumice lapilli beds with undifferentiated fluvial sedimentary structures, situated on sloping urban terrain. At measurement point I12 (Gamalama Mt., Ternate City, Indonesia), the natural resonance frequency (f_c) of 16.14 Hz is identified, corresponding to Tertiary or older hard sandy rocks, gravel, and similar deposits (Table 2; Fig. 7a). The shear wave velocity profile is delineated as follows: (1) 92 m/s at shallow depths (≤1.4 m), classified as soft soil; (2) 218 m/s at depths of 1.4–4 m, representing medium soil; (3) 311 m/s at intermediate depths (4–20 m), indicating medium soil; and (4) 645 m/s at greater depths (20–30 m), consistent with hard soil/soft rock formations (Table 1; Fig. 7b).

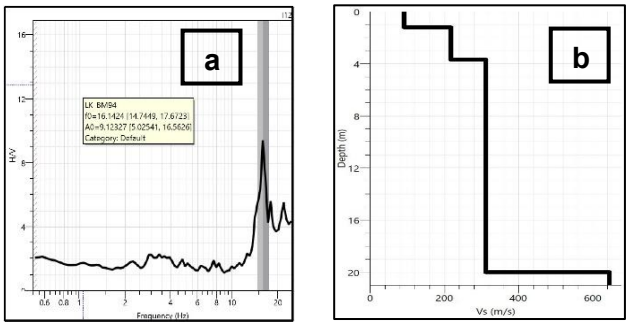

Figure 7. Observations at point I12. (a) HVSR spectrum. (b) V_S Model

Geological structure identification was conducted in the densely populated area of the Old Gamalama volcanic complex, which is composed of lava, lahar deposits, and pyroclastic materials. Eighteen cross-sections (A-F), each spanning 4.82 km, and one additional section (G1) measuring 1.85 km were established.

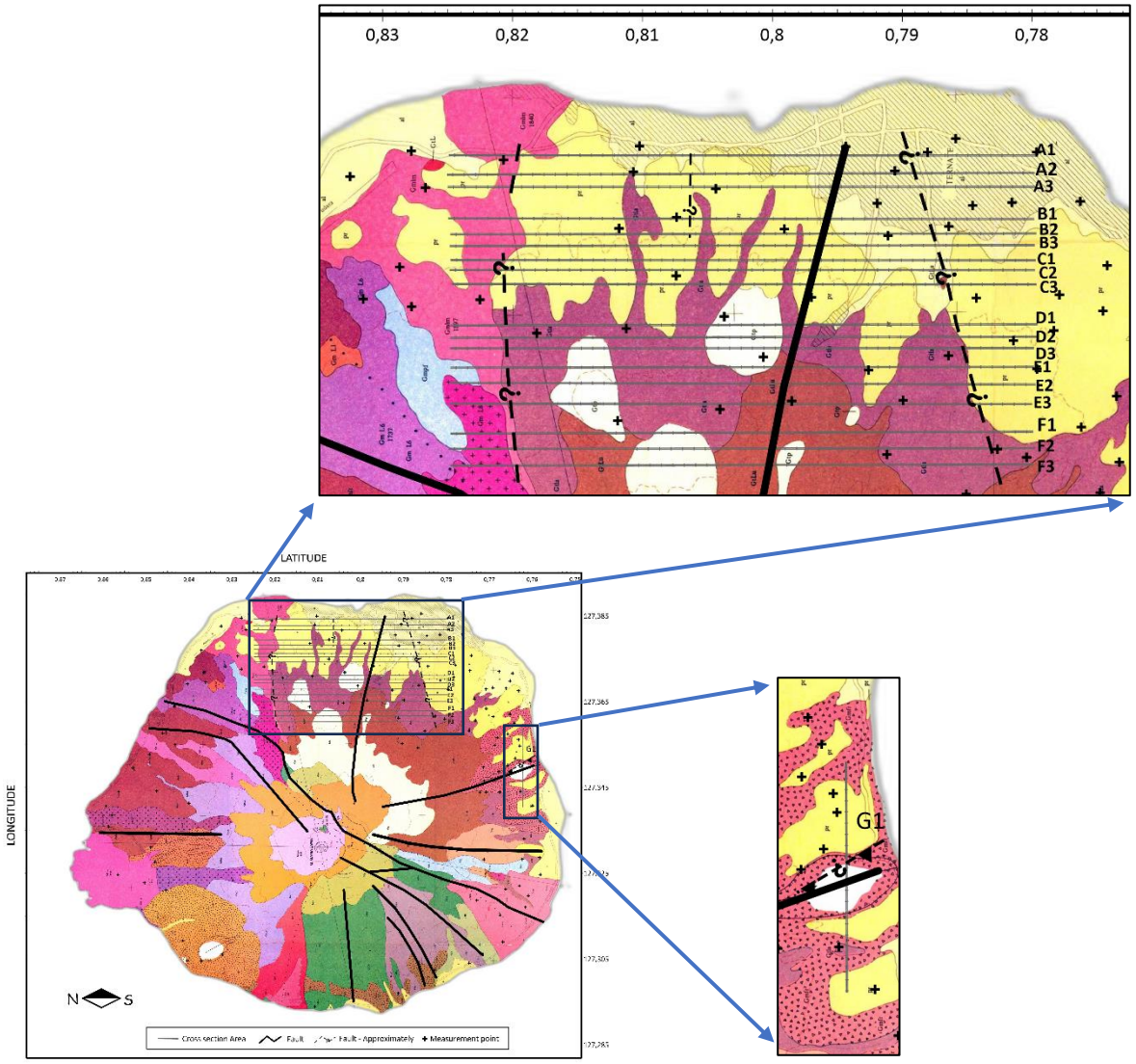

Figure 8. Modification of geological maps [5] and active faults. The determination of active faults in the map is based on morphological appearances using GoogleEarth satellite imagery [2]

Layer thickness interpolation revealed suspected fault traces, leading to the identification of four E-W striking faults (H, I, J, K) and one N-S striking fault (L). Faults J and L were determined based on satellite imagery morphology [12] and verified through layer thickness data, while faults H, I, and K were derived from thickness variation interpretation. Fault H was observed across all sections except B1-B3, exhibiting an E-W strike precisely at the boundary between old (Gt) and young (Gm) lahar deposits, partially overlain by surface sediments. Fault I, with a short E-W striking segment, was detected only in sections A1-A3 and B1-B3, predominantly buried under surface deposits. Faults J and K were clearly identified in all sections with consistent E-W trends. Fault L, constrained by limited data, was mapped through a single cross-section and intersects Ngade Maar, as documented in geological records.

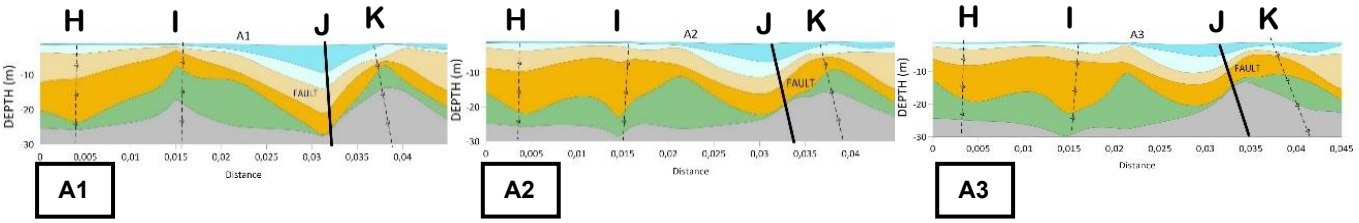

Figure 9. Cross Section A1-A2-A3

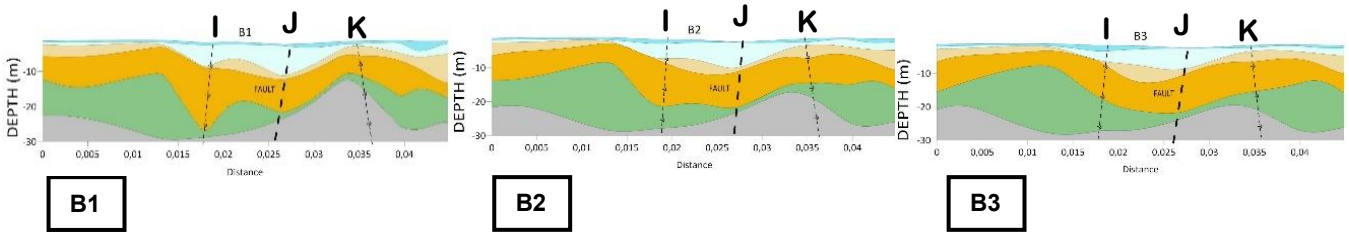

Figure 10. Cross Section B1-B2-B3

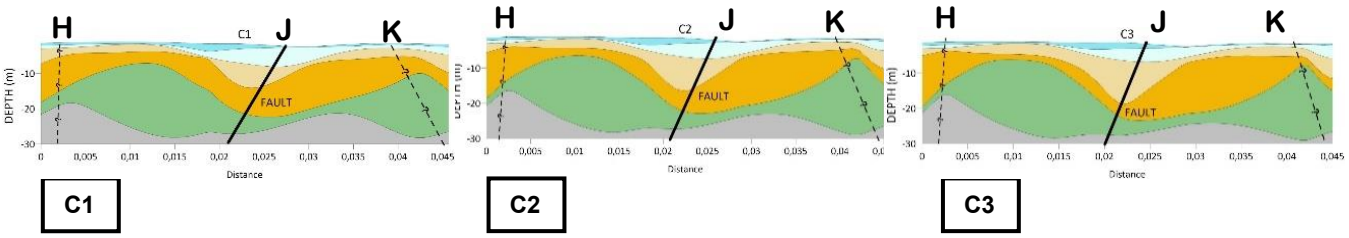

Figure 11. Cross Section C1-C2-C3

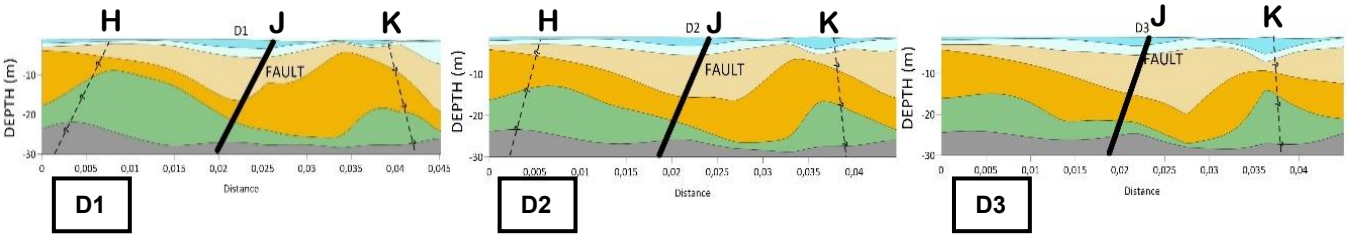

Figure 12. Cross Section D1-D2-D3

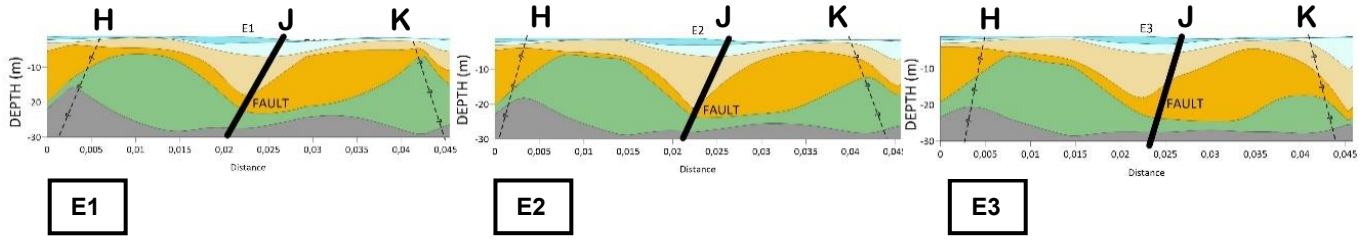

Figure 13. Cross Section E1-E2-E3

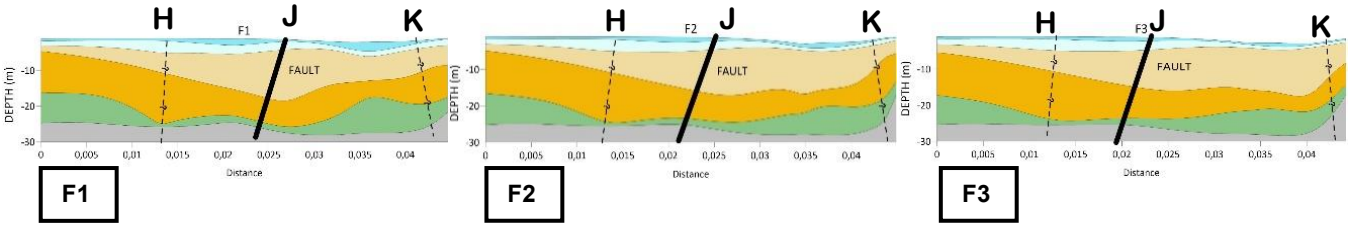

Figure 14. Cross Section F1-F2-F3

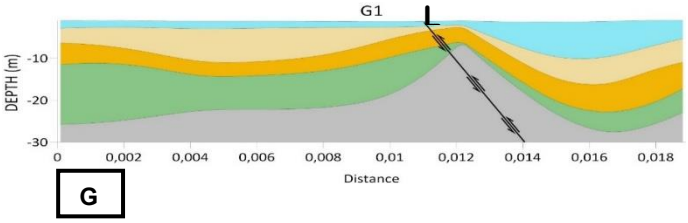

Figure 15. Cross Section G1

Conclusions

In conclusion, faults H, I, J, K, and L were identified through the interpretation of layer thickness from HVSR inversion at 0-30 m depth, with cross-sectional morphology and geology of Gamalama Volcano being compared for validation.

These fault manifestations are attributed to multiple factors: (1) thermal cracking during lava cooling, which reduces rock strength and increases volcanic susceptibility to deformation and faulting [28], [29]; (2) hydrothermal system pressure changes causing rock fracturing through thermal expansion, forming minor faults [30], [31]; (3) volcanic stress and tectonic strain influencing fault patterns [32]; and (4) gravitational collapse of steep volcanic slopes generating normal or detachment faults [33]. The fault presence implies potential seismic implications, where fluid temperature-pressure variations along faults may affect earthquake nucleation [30], while stress field modifications from tectonic strain or magma intrusions can reactivate pre-existing faults or initiate new ones [32].

Conflicts of Interest

The authors declare that there is no conflict of interest regarding the publication of this paper.

Acknowledgment

We extend our sincere gratitude to the Instrument Standardization Center of MKG–BMKG and the Ternate Geophysical Station, Indonesia, for their valuable assistance and for supplying the seismograph equipment used in this study.

References

[1] Clor, L. E., Fischer, T. P., Hilton, D. R., Sharp, Z. D., & Hartono, U. (2005). Volatile and N isotope chemistry of the Molucca Sea collision zone: Tracing source components along the Sangihe Arc, Indonesia. *Geochemistry, Geophysics, Geosystems, 6*(3). https://doi.org/10.1029/2004GC000825.

[2] Kunrat, S., Bani, P., Haerani, N., Saing, U. B., Aiuppa, A., & Syahbana, D. K. (2020). First gas and thermal measurements at the frequently erupting Gamalama volcano (Indonesia) reveal a hydrothermally dominated magmatic system. *Journal of Volcanology and Geothermal Research, 407*, 107096. https://doi.org/10.1016/j.jvolgeores.2020.107096.

[3] Obermann, A., Planès, T., Larose, E., & Campillo, M. (2013). Imaging preeruptive and coeruptive structural and mechanical changes of a volcano with ambient seismic noise. *Journal of Geophysical Research: Solid Earth, 118*(12), 6285–6294. https://doi.org/10.1002/2013JB010399.

[4] Venzke, E. (Comp.). (2024). *Volcanoes of the world* (Version 5.2.8; May 6, 2025). Smithsonian Institution. https://doi.org/10.5479/si.GVP.VOTW5-2024.5.2.
[5] Bronto, S., Hadisantoso, R. D., & Lockwood, J. P. (1982). *Peta Geologi Gunungapi Gamalama, Ternate, Maluku Utara*. Direktorat Vulkanologi, Indonesia.
[6] Montanaro, C., *et al.* (2022). Phreatic and hydrothermal eruptions: From overlooked to looking over. *Bulletin of Volcanology, 84*(6). https://doi.org/10.1007/s00445-022-01571-7.
[7] Stix, J., & de Moor, J. M. (2018). Understanding and forecasting phreatic eruptions driven by magmatic degassing. *Earth, Planets and Space, 70*(1). https://doi.org/10.1186/s40623-018-0855-z.
[8] Ceballo, R. M., González Herrera, R., Paz Tenorio, J. A., Aguilar Carboney, J. A., & Del Carpio Penagos, C. U. (2019). Effects of sediment thickness upon seismic amplification in the urban area of Chiapa de Corzo, Chiapas, Mexico. *Earth Sciences Research Journal, 23*(2), 111–117. https://doi.org/10.15446/esrj.v23n2.72623.
[9] Hutchison, W., *et al.* (2023). Gas emissions and subsurface architecture of fault-controlled geothermal systems: A case study of the North Abaya geothermal area. *Geochemistry, Geophysics, Geosystems, 24*(4), e2022GC010822. https://doi.org/10.1029/2022GC010822.
[10] Malusà, M. G., Brandmayr, E., Panza, G. F., Romanelli, F., Ferrando, S., & Frezzotti, M. L. (2022). An explosive component in a December 2020 Milan earthquake suggests outgassing of deeply recycled carbon. *Communications Earth & Environment, 3*(5), 5. https://doi.org/10.1038/s43247-021-00336-y.
[11] Oliva, S. J., *et al.* (2019). Insights into fault-magma interactions in an early-stage continental rift from source mechanisms and correlated volcano-tectonic earthquakes. *Geophysical Research Letters, 46*, 2065–2074. https://doi.org/10.1029/2018GL080866
[12] Nakamura, Y. (1989). *Method for dynamic characteristics estimation of subsurface using microtremor on the ground surface*.
[13] Sokolov, V. Y., Loh, C.-H., & Jean, W.-Y. (2007). Application of horizontal-to-vertical (H/V) Fourier spectral ratio for analysis of site effect on rock (NEHRP-class B) sites in Taiwan. *Soil Dynamics and Earthquake Engineering, 27*(4), 314–323. https://doi.org/10.1016/j.soildyn.2006.09.001.
[14] Arai, H., & Tokimatsu, K. (2005). S-wave velocity profiling by joint inversion of microtremor dispersion curve and horizontal-to-vertical (H/V) spectrum. *Bulletin of the Seismological Society of America, 95*(5), 1766–1778. https://doi.org/10.1785/0120040243.
[15] Okada, H. (2003). *The microtremor survey method*. Society of Exploration Geophysicists. https://books.google.co.id/books?id=aj1NAQAAIAAJ.
[16] Picotti, S., Francese, R., Giorgi, M., Pettenati, F., & Carcione, J. M. (2017). Estimation of glacier thicknesses and basal properties using the horizontal-to-vertical component spectral ratio (HVSR) technique. *Journal of Glaciology, 63*(238), 229–248. https://doi.org/10.1017/JOG.2016.135.
[17] Tian, B., Du, Y., You, Z., & Zhang, R. (2019). Measuring the sediment thickness in urban areas using revised H/V spectral ratio method. *Engineering Geology*, 105223. https://doi.org/10.1016/j.enggeo.2019.105223.
[18] Thein, P., Pramumijoyo, S., Brotopuspito, K. S., Kiyono, J., Wilopo, W., & Setianto, A. (2014). Microtremors HVSR correlation with sub surface geology and ground shear strain at Palu City, Central Sulawesi Province, Indonesia. *International Journal of Innovation in Science and Mathematics, 2*(5).
[19] Sambridge, M. (1999). Geophysical inversion with a neighbourhood algorithm—I. Searching a parameter space. *Geophysical Journal International, 138*(2), 479–494. https://doi.org/10.1046/j.1365-246X.1999.00876.x.
[20] SESAME Project. (2004). *Guidelines for the implementation of the H/V spectral ratio technique on ambient vibrations: Measurements, processing, and interpretations*. http://sesame.geopsy.org/Delivrables/Del-D23-HV_User_Guidelines.pdf.
[21] Konno, K., & Ohmachi, T. (1998). Ground-motion characteristics estimated from spectral ratio between horizontal and vertical components of microtremor. *Bulletin of the Seismological Society of America, 88*(1), 228–241. https://doi.org/10.1785/bssa0880010228.
[22] Wathelet, M., *et al.* (2020). Geopsy: A user-friendly open-source tool set for ambient vibration processing. *Seismological Research Letters, 91*(3), 1878–1889. https://doi.org/10.1785/0220190360.
[23] Schön, J. H. (2011). *Physical properties of rocks: A workbook* (Vol. 8). Elsevier.
[24] Badan Standardisasi Nasional. (2012). *SNI 1726:2012: Tata cara perencanaan ketahanan gempa untuk struktur bangunan gedung dan non gedung*. http://www.bsn.go.id.
[25] Tarantola, A. (2005). *Inverse problem theory and methods for model parameter estimation*. Society for Industrial and Applied Mathematics.
[26] Sanchez-Brea, L. M., & Bernabeu, E. (2005). Effect of noise in the estimation of magnitudes with spatial dependence: A spatial statistics technique based on kriging. *AIP Conference Proceedings, 780*, 811–814. https://doi.org/10.1063/1.2036872.
[27] Riyanto, D. P., Dhanardono, B., Suhardi, Prasetyo, W., Apriyoga, W., & Yulianto, G. (2025). The HVSR analysis for determining the seismic vulnerability and soil characteristics of the Randugunting Dam. *IOP Conference Series: Earth and Environmental Science*, 12011. https://doi.org/10.1088/1755-1315/1467/1/012011.
[28] Browning, J., Meredith, P., & Gudmundsson, A. (2016). Cooling-dominated cracking in thermally stressed volcanic rocks. https://doi.org/10.1002/2016GL070532.
[29] Lamur, A., *et al.* (2018). Disclosing the temperature of columnar jointing in lavas. *Nature Communications, 9*(1), 1432. https://doi.org/10.1038/s41467-018-03842-4.
[30] Sutherland, R., *et al*. (2017). Extreme hydrothermal conditions at an active plate-bounding fault. *Nature, 546*(7656), 137–140. https://doi.org/10.1038/nature22355.
[31] Yamashita, T. (1999). Pore creation due to fault slip in a fluid-permeated fault zone and its effect on seismicity. In M. Wyss, K. Shimazaki, & A. Ito (Eds.), *Seismicity patterns, their statistical significance and physical meaning* (pp. 625–647). Birkhäuser Basel. https://doi.org/10.1007/978-3-0348-8677-2_19.
[32] Aoki, Y. (2022). Earthquake focal mechanisms as a stress meter of active volcanoes. *Geophysical Research*

Letters, 1–5. https://doi.org/10.1029/2022GL100482.
[33] Di, F., Matteo, T., Alessandro, R., & Felix, B. (2020). Editorial: Flank dynamics, sector collapses, lahars, and rockfalls: Analysis, monitoring, and modelling of volcanic slope instability. *Frontiers*, 2615–2618.